



## Effects of polytetrafluoroethylene treatment and compression on gas diffusion layer microstructure using high-resolution X-ray computed tomography

Navvab Khajeh-Hosseini-Dalasm<sup>a,1</sup>, Takashi Sasabe<sup>a,b</sup>, Takashi Tokumasu<sup>c</sup>, Ugur Pasaogullari<sup>a,\*</sup>

<sup>a</sup> Department of Mechanical Engineering, and Center for Clean Energy Engineering, University of Connecticut, Storrs, CT 06269-5233, USA

<sup>b</sup> Department of Mechanical and Control Engineering, Tokyo Institute of Technology, O-okayama, Meguro-ku, Tokyo 152-8552, Japan

<sup>c</sup> Institute of Fluid Science, Tohoku University, Sendai, Miyagi 980-8577, Japan



### HIGHLIGHTS

- The microstructure of a TGP-H-120 gas diffusion layer (GDL) was investigated using high resolution X-ray CT technique.
- A sample holder was designed to investigate the effects of non-uniform compression pressure.
- Anisotropic microstructure, nonuniform PTFE distribution, and significant microstructural change with compression were seen.
- At 3 MPa, 16% reduction is bulk porosity and a large penetration of GDL into the channel (132  $\mu$ m) was observed.

### ARTICLE INFO

#### Article history:

Received 21 January 2014

Received in revised form

25 April 2014

Accepted 2 May 2014

Available online 13 May 2014

#### Keywords:

Gas diffusion layer

Microstructure

X-ray computed tomography

Non-uniform compression pressure

### ABSTRACT

The microstructure of a TGP-H-120 Toray paper gas diffusion layer (GDL) was investigated using high resolution X-ray computed tomography (CT) technique, with a resolution of 1.8  $\mu$ m and a field of view (FOV) of  $\sim 1.8 \times 1.8$  mm. The images obtained from the tomography scans were further post processed, and image thresholding and binarization methodologies are presented. The validity of Otsu's thresholding method was examined. Detailed information on bulk porosity and porosity distribution of the GDL at various Polytetrafluoroethylene (PTFE) treatments and uniform/non-uniform compression pressures was provided. A sample holder was designed to investigate the effects of non-uniform compression pressure, which enabled regulating compression pressure between 0, and 3 MPa at a gas channel/current collector rib configuration. The results show the heterogeneous and anisotropic microstructure of the GDL, non-uniform distribution of PTFE, and significant microstructural change under uniform/non-uniform compression. These findings provide useful inputs for numerical models to include the effects of microstructural changes in the study of transport phenomena within the GDL and to increase the accuracy and predictability of cell performance.

© 2014 Elsevier B.V. All rights reserved.

## 1. Introduction

Polymer electrolyte fuel cells (PEFCs) are among the promising clean energy conversion technologies which convert the chemical

energy of hydrogen fuel to electricity directly, with byproducts of only heat and water, which need to be removed from the fuel cell effectively. Otherwise, membrane dry out and/or flooding can take place, which lead to increased ionic resistance and/or mass transport loss, respectively. This is more pronounced especially when operating at high current densities as the heat generation and liquid water production are considerably higher.

High current density operation is drawing attention especially for automotive applications as it maximizes power generation and consequently lowers the size and cost of the fuel cell systems. The design of PEFC components should be optimized to enable

\* Corresponding author. 44 Weaver Rd, U-5233, Storrs, CT 06269-5233, USA. Tel.: +1 860 486 9441.

E-mail address: [ugur.pasaogullari@uconn.edu](mailto:ugur.pasaogullari@uconn.edu) (U. Pasaogullari).

<sup>1</sup> Current address: Aerosol Dynamics & Respiratory Transport Research Lab, Virginia Commonwealth University, Richmond, VA 23284-3015, USA. Tel.: +1 804 828 9117.

effective removal of excessive heat and water, in which the GDL becomes a key component. GDLs serve many purposes in a PEFC: they distribute the reactants from the gas channels to active reaction sites, and collect the reactions products from active reaction sites and transport to gas channels. They also facilitate conduction of electrons to and from the active reaction sites, and remove the heat from the polymer electrolyte membrane (PEM) and catalyst layers.

GDLs are typically made of conductive material, and in many cases are even treated with hydrophobic agents (e.g. polytetrafluoroethylene, PTFE) to facilitate liquid water removal to gas channels, which is shown to affect the microstructure of GDLs [1]. Moreover, GDLs are assembled under high compression pressures to minimize the contact resistance between the components [2]. Due to the channel-rib configuration of bipolar plates (also called separator plates or flow fields) the compression applied to the GDL is non-uniform, which affects the GDL microstructure under rib and channel differently and results in an in-plane variation of the microstructure. Transport phenomena in GDL such as capillary transport of liquid water and gas phase diffusion are significantly affected by the microstructural properties of the GDL including bulk porosity and porosity distribution [3,4]. In order to understand the microstructure-transport property relationships, it is necessary to characterize the GDL microstructure, particularly at various PTFE treatment conditions and non-uniform compression pressure.

There have been recent studies for full scale microstructural visualization of PEM fuel cell porous materials using various techniques, including X-ray computed tomography (CT) and focused ion beam scanning electron microscopy (FIB-SEM). There have been several studies focusing on FIB-SEM technique for characterization of porous materials used in fuel cells [5–10]. The FIB-SEM technique has the highest spatial resolution, currently at  $\sim 20$  nm. However, it is a destructive technique and is used for very small samples (i.e. few-microns). Obtaining good contrast between phases in FIB-SEM is strongly dependent on electron beam energy, detector type and the phases involved [11]. For PEFCs, FIB-SEM has been applied to micro-porous layers, and digital reconstruction of microstructure and key transport properties such as tortuosity and diffusivity were obtained [12]. FIB-SEM technique was also applied to catalyst layers, and the surface area of platinum catalyst was analyzed [13].

X-ray CT, on the other hand is a non-destructive method with resolutions of  $\sim 1$   $\mu$ m for micro X-ray CT ( $\mu$ XCT), and  $\sim 20$  nm for nano X-ray CT (NCT).  $\mu$ XCT has been used for microstructure properties quantification of PEM fuel cell GDLs [14,15]. Wargo et al. [14] investigated a GDL microstructure and provided a detailed discussion on transport-structure properties such as bulk porosity, pore connectivity, tortuosity, diffusivity, permeability and capillary pressure-saturation curves using sets of 300 random volumes with equal sizes of  $\sim 1$   $\mu$ m<sup>3</sup>. Pfrang et al. [15] applied X-ray CT for 3D imaging of an MEA assembly including SGL-31BC GDLs on either side of the catalyst coated membrane (CCM). They visualized the fibrous structure of the GDL and the density of micro cracks present in CLs. The heterogeneous porosity of GDL was first reported by Buchi et al. [16] by showing porosity distribution in through thickness direction using  $\mu$  X-ray CT with 1  $\mu$ m resolution for a TGP-H-060 GDL with 20% PTFE treatment. For several other types of GDLs such as Toray, SGL Sigracet and E-Tek ELAT, the heterogeneous microstructure was investigated by Fishman et al. [17,18] in both through thickness and in-plane directions. In an operating PEM fuel cell, GDLs are under compression, which alters their microstructure. The effects of uniform compression on GDL microstructure was investigated by Becker et al. [19] with a Toray TGP-H-060 carbon paper GDL.

As noted earlier, due to rib and channel configuration of bipolar plates, GDLs are under non-uniform compression pressure in PEFC assembly. The effect of non-uniform compression was only recently studied by James et al. [20] on SGL Sigracet GDL 30BA. However, in their study compression was obtained by changing the sample thickness and therefore the amount of compression pressure was neither controlled nor measured and the compression on the sample was uniform.

In this study, using a high resolution  $\mu$ XCT technique we present the effects of PTFE treatment and uniform/non-uniform compression pressure on the microstructure of a carbon paper GDL (i.e. Toray<sup>®</sup> TGP-H-120). A sample holder is designed, which is equipped with spring, spacers, and rod to enable adjusting the compression pressure. For the study of non-uniform compression pressure on the GDL microstructure, a rod which has a channel-rib configuration was used. The  $\mu$ XCT technique provided 3D microstructural data for image processing using Avizo (FEI Visual Sciences Group, Burlington, MA) and ImageJ [21–23]. The details of image processing procedure are provided. The validation of commonly used Otsu's thresholding method versus thresholding based on bulk porosity measured by mercury intrusion porosimetry (MIP) is examined. Next, the results on heterogeneous anisotropic porosity distribution of the GDL are shown and then the effects of the following aspects on the GDL microstructure are investigated: 1) PTFE treatment, 2) uniform compression pressure, and 3) non-uniform compression pressure.

## 2. Experimental methodology

### 2.1. X-ray CT

Micro X-ray Computed Tomography,  $\mu$ XCT (Micro XCT-400, Xradia, Concordia, CA) is used to non-destructively obtain the microstructure of a GDL (TGP-H-120 Toray paper). The X-ray CT system is mainly composed of an X-ray source, a sample stage, and a detector. The X-rays source used in this study has an energy range of 20–90 keV and power range of 1–8 W. The sample-detector and source-sample distances were set as, 10 mm and 20 mm, respectively. Resolutions of the detector optics and magnification ratio of the imaging are the key factors for high resolution imaging. In conventional laboratory-based X-ray systems, the beam is cone shaped and the geometrical magnification ratio (MR) of the beam is defined by [24]:

$$MR = \frac{SOD}{SID} \quad (1)$$

where SOD is the source to object distance and SID is the source to image distance (see Fig. 1). A larger SOD results in higher magnification but lowers the imaging spatial resolution. This issue is resolved with high-resolution X-ray CT systems by Carl Zeiss X-ray Microscopy (Pleasanton, CA, formerly known as Xradia, Inc.). In this study, the  $\times 10$  magnification lens is mainly used, the field of view is  $1.8 \times 1.8$  mm, and the spatial resolution is 1.8  $\mu$ m.

Absorption contrast is obtained due to variation of the attenuation of X-rays in different materials, characterized by the attenuation coefficient [24]. The absorption contrast relates to mass attenuation coefficient and material density, the attenuation is governed by Beer's law:

$$\frac{I}{I_0} = \exp[-\mu x] = \exp\left[\left(-\frac{\mu}{\rho}\right)\rho x\right] \quad (2)$$

where  $I_0$  is the initial X-ray intensity,  $I$  is the detected X-ray intensity,  $\mu/\rho$  is the mass attenuation coefficient, and  $x$  is the X-ray

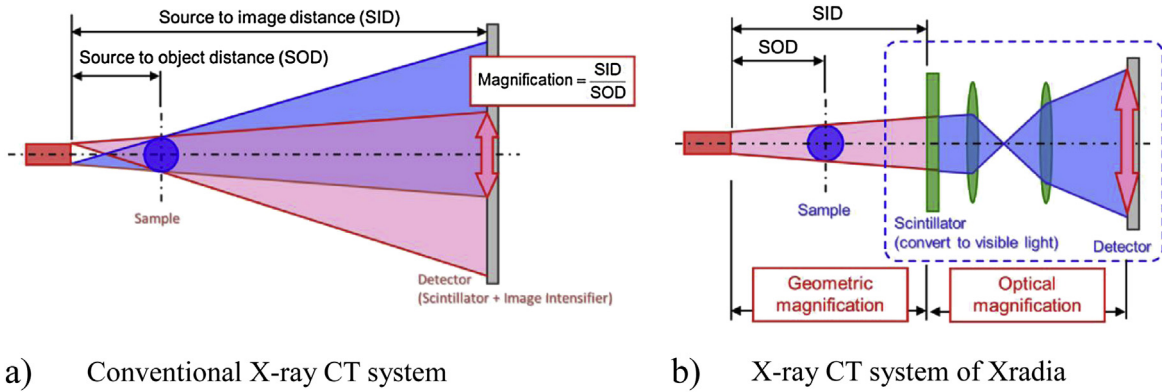


Fig. 1. Magnification mechanisms of X-ray CT system.

path length through the material. Since the attenuation coefficient of air and the GDL materials are different, there is a contrast in the absorption of X-rays between the solid phase and the open pore phase, which enables imaging of the pore structure.

For each sample, 1000 projections over  $180^\circ$  were obtained, with exposure time of 10 s, resulting in a total scanning time of 6 h per sample. It is found that an accelerating voltage of 20 keV and tube current of  $200 \mu\text{A}$  provides the optimal contrast. A visualization of the GDL microstructure is shown in Fig. 2.

### 2.1.1. Sample holder

A sample holder is designed, which is equipped with a spring and spacers to precisely regulate the compression pressure applied on the sample as shown in Fig. 3. The compression can be adjusted by choosing the spring and its length displacement. The sample holder is made of PEEK, which has an attenuation coefficient different from the GDL material and air; therefore the GDL can be easily distinguished from the sample holder at the image processing stage. The sample holder is also designed to provide a short source to image distance, SID for a higher geometrical magnification and less artifacts, e.g. blurring. As it can be seen in Fig. 3, a 3 mm in diameter sample is placed between two compression rods. In case of channel/rib configuration, a rod, with a machined slit on one side is used. In the current work, spring constants of 2.9 and  $5.9 \text{ N mm}^{-1}$  are chosen to regulate compression pressures of 1, 2, and 3 MPa.



Fig. 2. Microstructural visualization of a TGP-H-120 Toray paper.

### 2.2. Mercury intrusion porosimetry

A mercury intrusion porosimetry (MIP) equipment (Autopore IV, Micromeritics Instruments) is utilized to determine the bulk porosity of the GDL samples. Four TGP-H-120 Toray papers (with PTFE treatments of 0, 10, 20, and 30 wt%) are characterized by MIP. The sample weight for each measurement was approximately 0.5 g. In MIP, the bulk porosity is obtained by measuring the volume of mercury penetrating into the sample and sample's weight. Table 1 summarizes the samples bulk porosities obtained by MIP. In this study the bulk porosity obtained from MIP is used to find a threshold value for X-ray CT image reconstruction.

### 3. Image processing

Images obtained from the micro X-ray CT scans are in 16-bit grayscale, with a range of 0–65,536. Open pores (i.e. air) and solid material should be separated, i.e. the grayscale images should be binarized. In Fig. 4, the image processing steps are demonstrated. First an image filter is used in order to reduce noises without significant degradation of resolution. A non-local means filter is utilized in this case (Fig. 4-b). After filtration, a threshold value for binarization needs to be specified. Microstructural properties such as pore size distribution and bulk porosity are sensitive to the specified threshold value as shown by Refs. [10,17,25–27]. For example, 1 bit grayscale change in threshold value results 0.43% change in the porosity value in an 8 bit image [10].

There are multiple methods to determine the threshold value. Threshold value can be estimated from the image histogram, by using the multiple distributions, which are indicators for different

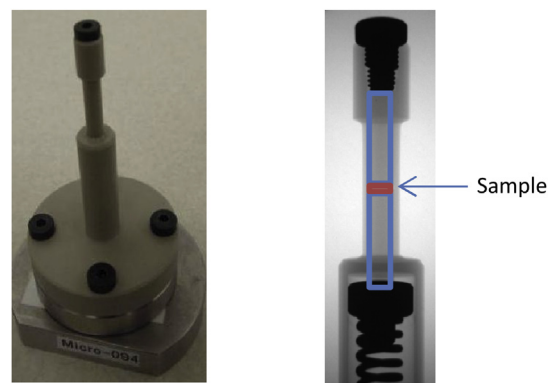


Fig. 3. Sample holder and compression mechanism.

**Table 1**

Bulk porosity obtained by mercury intrusion porosity (MIP) for TGP-H-120 Toray paper GDLs with different PTFE percentages.

PTFE %	0	10	20	30
Bulk porosity	72.2	66.2	64.1	60.2

materials present in the sample. However, as shown in Fig. 5-a, the GDL histogram does not show a clear distinction. Another alternative way for selecting the threshold value is to plot the grayscale value along a line across the geometry. As it is shown in Fig. 5-b, the boundaries between different materials are ambiguous and cannot be easily distinguished. Several studies have used Otsu's method for automatic thresholding [17,20]. Otsu's method [28] calculates threshold value between two materials so that their intra-class variance is minimum. However, Sezgin and Sankur [29] showed that the Otsu's method is not always reliable. In this study, we determine the threshold value, such that the calculated bulk porosity agrees with the bulk porosity obtained with MIP. Bulk porosities for TGP-H-120 Toray paper with different PTFE treatment obtained by MIP were shown in Table 1. For compressed GDLs, the bulk porosity can be obtained from the compressed and uncompressed thicknesses as:

$$\varepsilon_c = 1 - (1 - \varepsilon) \left( \frac{l}{l_c} \right) \quad (3)$$

where  $\varepsilon_c$ ,  $\varepsilon$ ,  $l_c$  and  $l$  are bulk porosities and thicknesses for compressed and uncompressed GDLs. For the uncompressed untreated GDL the bulk porosity of 72.2% was obtained with a threshold grayscale value of 30,500, which is obtained by matching the bulk porosity measured by MIP, as explained above. Using Otsu's method a threshold value of 30,905 was obtained, which resulted in bulk porosity of 74.5%, overestimating by 3.2%. A binarized image is shown in Fig. 4-c. A grayscale value smaller than the threshold value has the value of 0 and is labeled black and a grayscale value greater than the threshold value has the value of 1 and is labeled white. In Fig. 4-c, the white region represents solid material and black region is pore space.

#### 4. Result and discussion

With image processing, the microstructural information of the untreated and treated TGP-H-120 Toray paper GDLs are obtained. In this section, first the porosity distribution of the untreated uncompressed GDL is discussed and then the effects of PTFE

treatment, uniform compression, and non-uniform compression on the GDL microstructure are investigated.

##### 4.1. Untreated and uncompressed GDL porosity distribution

For an untreated uncompressed TGP-H-120 Toray paper GDL, the porosity distribution along the thickness of the sample is shown in Fig. 6. The porosity at each slice is calculated by determining the number of pixels representing solid materials such as carbon fiber, binder, and PTFE and the total number of pixels:

$$\varepsilon = 1 - \frac{\text{solid pixels}}{\text{total pixels}} \quad (4)$$

It is seen that the porosity distribution is heterogeneous with significant variation in local porosity across the thickness of the sample (i.e., across the fiber layers). Inside the GDL, the maximum porosity decrease and increase are approximately 8% and 10%, respectively. The bulk porosity  $\varepsilon_{\text{bulk}}$  is also shown in Fig. 6, which represents average porosity distribution over the entire thickness. Kong et al. [30] verified that the porosity distribution is more important than bulk porosity. However, most of the numerical studies only use the bulk porosity due to simplicity [28–34] and effects of the porosity distribution need further investigation. Heterogeneous porosity distribution of the untreated sample seen in Fig. 6 is attributed to non-uniform binder coverage within the sample and manufacturing processes such as “molding” and “hydroentanglement” as explained in Refs. [35,17]. However, it was not possible to show the non-uniform distribution of binder due to similar attenuation between the carbon fibers and the binder as well as the resolution. In addition, that the sample's volume is  $1.8 \times 1.8 \times 1.8 \text{ mm}^3$ , which is bigger than the minimum representative volume to capture a GDL porosity distribution based on Fishman et al. [17].

In Fig. 6, the porosity distribution in in-plane direction is also shown. Compared to the through thickness porosity distribution, in-plane porosity distribution is less heterogeneous. Its variation is between 2% lower to 3% higher than the average bulk porosity value. This also suggests that the assumption of uniform porosity distribution is more valid in in-plane direction compared to through thickness direction. More uniform porosity distribution in the in-plane direction is due to the orientation of the carbon fibers as layers in through-plane direction. The comparison proves anisotropy in porosity distribution for the untreated TGP-H-120 Toray paper GDL. The anisotropic porosity distribution is an indication for anisotropy in transport properties, which is numerically [36–38] and experimentally [39,40] investigated and was shown to affect transport phenomena including water and thermal management in PEM fuel cells. However, these numerical studies

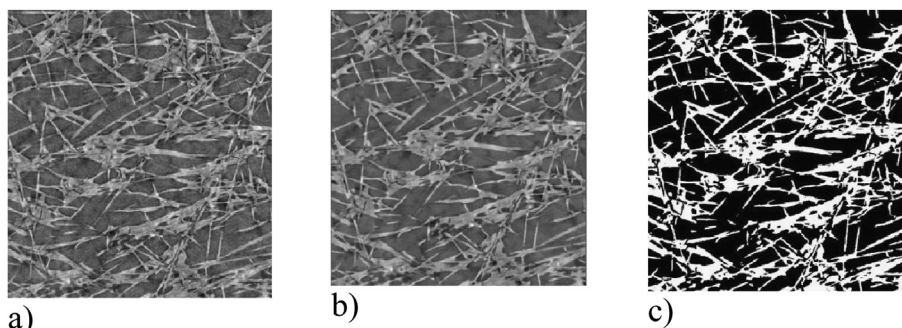


Fig. 4. Image processing steps, a) raw image, b) filtered image, and c) binarized image.

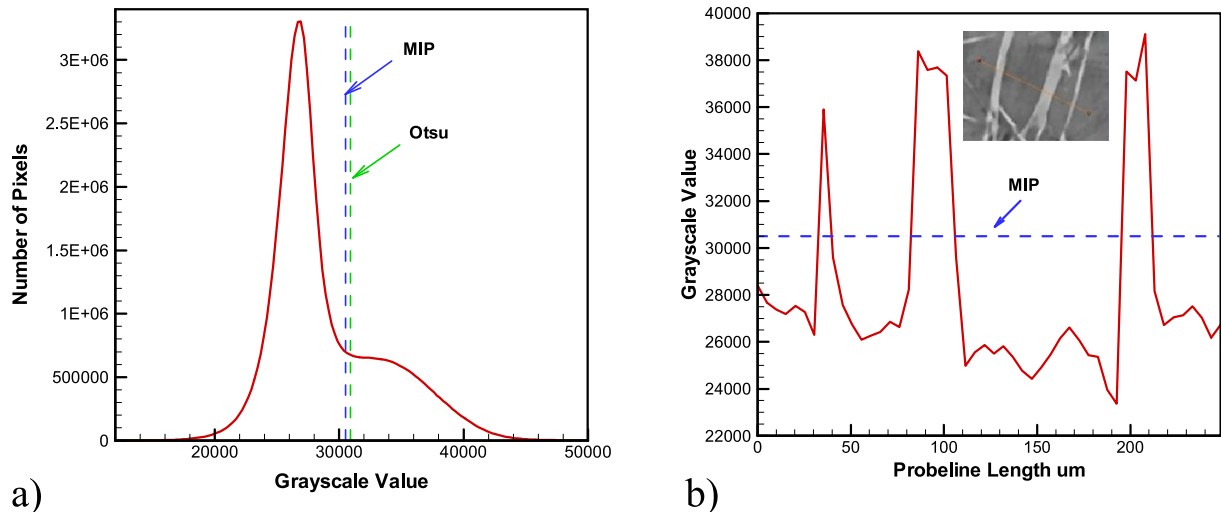


Fig. 5. a) Histogram plot for an untreated uncompressed TGP-H-120 Toray paper GDL with MIP and Otsu threshold values, and b) grayscale (intensity) value plot along a probe line.

assume uniform porosity and do not consider the effects of heterogeneous porosity distribution.

#### 4.2. Effect of PTFE treatment

Fig. 7 shows porosity distribution and bulk porosity for uncompressed TGP-H-120 Toray paper GDLs with different PTFE treatments: 0, 10, 20, and 30 wt % PTFE. As the hydrophobic PTFE agent is added to the GDL the bulk porosity decreases (see Fig. 7-b). A linear curve fit to the bulk porosity data is:

$$\varepsilon_{\text{PTFE}} = \varepsilon_0 + 0.38\text{PTFE\%} \quad (5)$$

where  $\varepsilon_0$  is the bulk porosity for the untreated TGP-H-120 Toray paper GDL. PTFE affects the GDL microstructure by reducing the bulk porosity, which increases the resistance to reactant transport and increases the electrical resistance due to lower conductivity of PTFE [41], whereas PTFE enhances removal of liquid water, minimizing flooding. Paganin et al. [42] found that the PTFE content of the gas diffusion layer has an optimal value at 15%. As shown in Fig. 7, the non-uniformity in local porosity increases with increase

in PTFE content, altering the distribution of large and small pores. This may affect the liquid water morphology as liquid water tends to flow through bigger pores in hydrophobic media ( $\theta > 90^\circ\text{C}$ ) due to lower entry pressure [1]. The non-uniformity of porosity distribution for an untreated GDL is mostly attributed to the binder distribution and for PTFE treated GDLs is more affected by PTFE distribution. In Fig. 7, for the 30% PTFE treated GDL the heterogeneous porosity distribution is more pronounced, especially near to the edges. The porosity distributions at different PTFE treatments show three peaks and four troughs, except for the 30% PTFE treatment. In addition, Fig. 7 shows that for the 30% PTFE treatment at one end there is an absolute minimum of local porosity value, which is as a result of highly nonuniform PTFE distribution. This can be visually confirmed with through-plane slices of the GDLs with different PTFE treatments, as shown in Fig. 8. In this grayscale image, the bright area represents solid material including fiber, binder and PTFE, and the dark area represents the pore region. There are high PTFE density regions at the bottom end, which correspond to the low local porosity as seen in Fig. 7. The non-uniform distribution of PTFE in the GDLs is related to PTFE coating process including chemical treatments, drying time length and thermal effects [43–45]. In addition, the highly non-uniform distribution of PTFE inside the GDL strongly impacts the liquid water distribution inside the GDL as a result of changes in pore size and hydrophobicity distribution [24]. Therefore, for realizing a high current density operation, more controlled PTFE treatment and further understanding of its impact on GDL transport phenomena becomes important. Recently, Inoue et al. [46] numerically studied the effects of drying process on PTFE distribution and concluded that a slower drying rate leads to a more controlled and uniform PTFE distribution. However, in their study the effect of PTFE coating process and PTFE particles size were not investigated.

#### 4.3. Effect of uniform compression

GDLs are compressed during an MEA assembly to obtain a better electrical contact resistance. However, with compression the GDLs' microstructure is affected. Fig. 9 displays the porosity distribution for three untreated TGP-H-120 Toray paper GDLs at uniform 1, 2, and 3 MPa compression pressure. As pressure is applied, sample is compressed; and consequently the thickness and the bulk porosity decrease. The change in thickness is attributed to complex stress-strain constitutive relationship of the GDL material. Bulk porosities

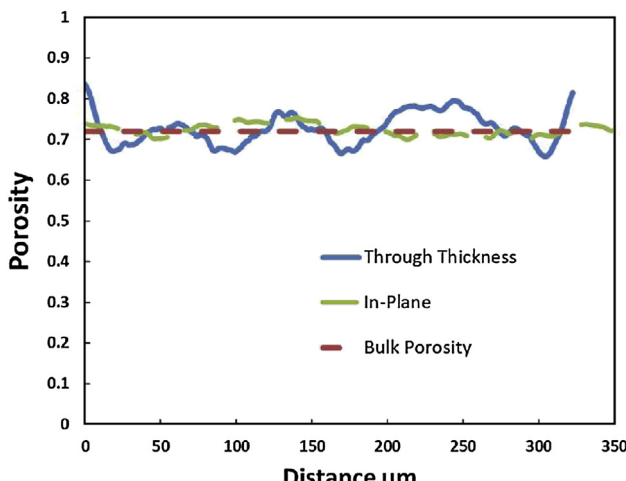


Fig. 6. Porosity distribution of an untreated TGP-H-120 Toray paper GDL in through thickness direction and it bulk porosity.

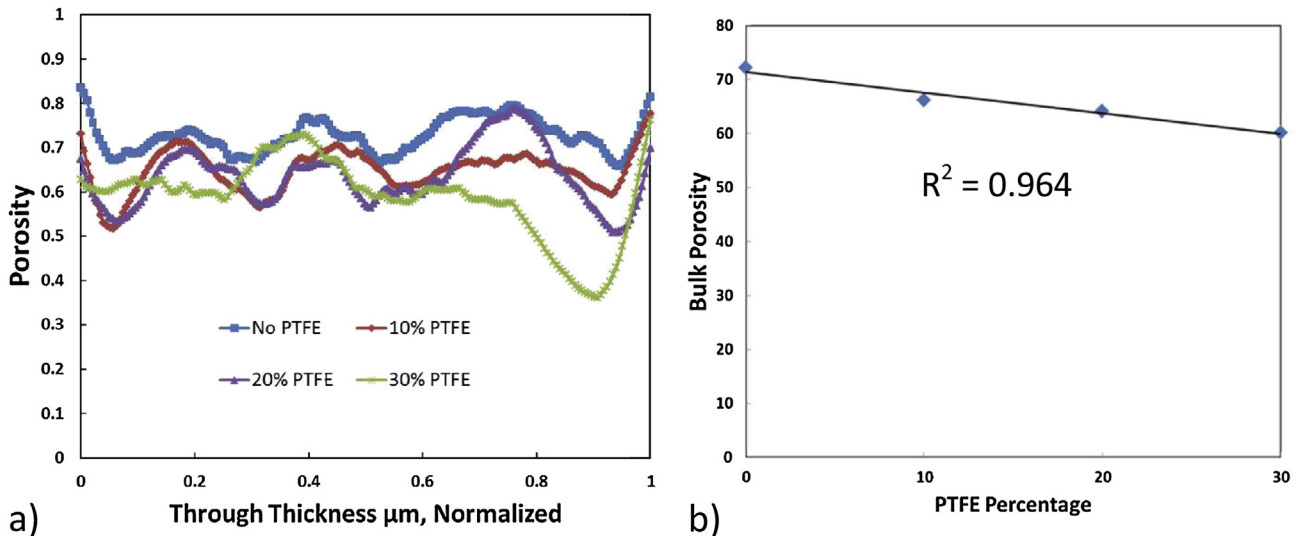


Fig. 7. a) Porosity distribution of TGP-H-120 Toray paper GDL at different PTFE treatments, and b) bulk porosity plot with PTFE treatment.

decreased by 3.0%, 6.6%, and 8.4% respectively at 1, 2, and 3 MPa compared to the uncompressed GDL porosity i.e. 72.2% (see Fig. 10 and Eq. (3)). The local porosity distribution also decreases with compressions. In Fig. 9, the lowest porosity is obtained at the 3 MPa compression pressure and is 17% lower the bulk porosity of the uncompressed GDL.

#### 4.4. Effect of non-uniform compression

The effects of uniform compression were shown in Figs. 9 and 10. However, at in-situ conditions, due to channel-rib configuration of bipolar plates, assembly pressure is applied to GDL non-uniformly. The effects of non-uniform compression pressure on an untreated TGP-H-120 Toray paper GDL's microstructure is investigated here using the sample holder shown in Fig. 3, which has a compression rod with a channel-rib configuration. The compression pressure is regulated with a spring and spacer. A spring with a constant number of  $5.9 \text{ N mm}^{-1}$  is selected and the compression pressure is tuned by the spacer thickness. The areas selected for porosity distribution measurement as well as a 3D visualization of rod/sample are shown in Fig. 11. The channel width is selected to be 1 mm. Fig. 12 shows the through thickness porosity distribution under rib and channel separately and at 1, 2, and 3 MPa

compression pressure. The average porosities under rib and channel are also shown in Fig. 12 and their values are reported in Table 2.

There are three main observations with increasing non-uniform compression pressure in Fig. 12a)-c). First, under channel and rib regions average porosity difference becomes larger. These average porosity reductions are 2.6%, 4.9%, and 16% at 1, 2, and 3 MPa, respectively. The significance of such an average porosity change on transport phenomena inside the GDL can be modeled by employing commonly used Tomadakis and Sotirchos (TS) relationship for the calculation of an effective gas diffusion coefficient ( $D^{\text{eff}}$ ) as:

$$\frac{D^{\text{eff}}}{D_{\text{bulk}}} = \varepsilon \left( \frac{\varepsilon - \varepsilon_p}{1 - \varepsilon_p} \right)^\alpha \quad (6)$$

where  $\varepsilon_p$  and  $\alpha$  are respectively the percolation threshold porosity and fitting parameter. Tomadakis and Sotirchos reported these values as  $\varepsilon_p = 0.11$  and  $\alpha = 0.785$  (through thickness) [47]. Using Eq. (6), for the high compression pressure of 3 MPa, 28.7% reduction in normalized gas effective diffusion between under channel and under rib region is calculated. Clearly, it can be seen that the accuracy of the numerical simulation with the same porosity value assumption under rib and channel is in doubt and the effects of non-uniform compression pressure on the GDL transport phenomena should be investigated. It is noted that the TS model here is

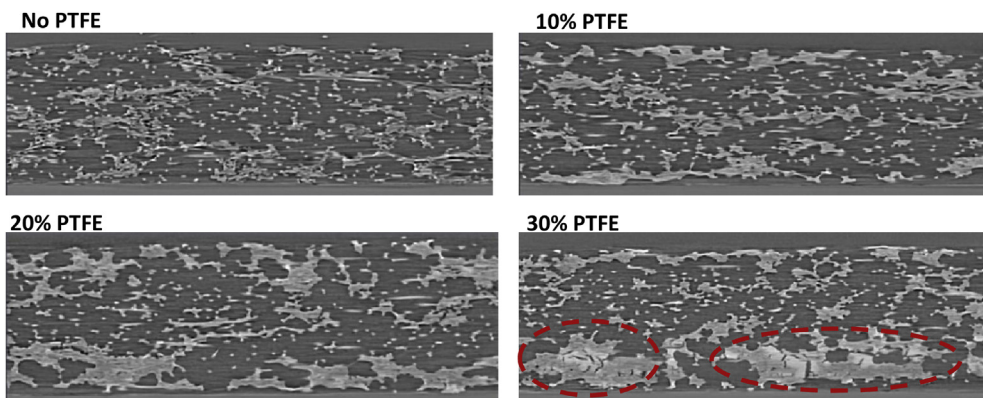


Fig. 8. Through thickness slices of TGP-H-120 Toray paper GDL with different PTFE treatment.

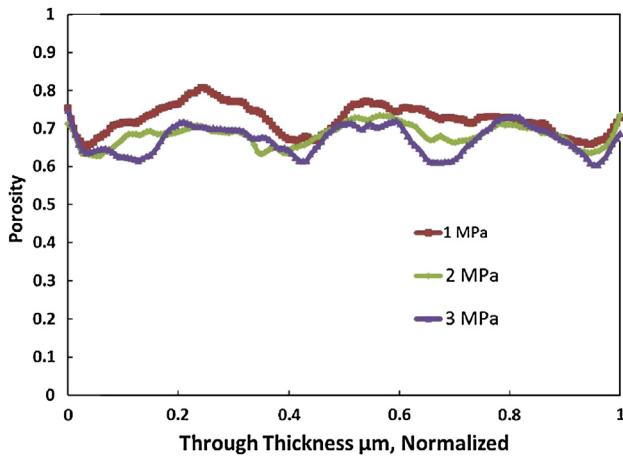


Fig. 9. Porosity distribution of untreated TGP-H-120 Toray paper GDLs at 1, 2, 3 MPa uniform compression pressures.

used for an estimate on the effects of compression pressure. The TS model is based on randomly oriented cylindrical fibrous porous media and may not be completely accurate for gas diffusion layers, for which the fibers are not exactly in cylindrical shape and randomly oriented.

The second observation in Fig. 12 is the penetration of the GDL material into the channel area as pressure increases. There is a small penetration of GDL material (measured to be 28  $\mu\text{m}$ ) into the channel at 1 MPa compression pressure. At higher compression pressures the GDL thickness difference under rib and channel increases. The penetration height in case of 2 and 3 MPa are measured as 61  $\mu\text{m}$  and 132  $\mu\text{m}$ , respectively. The penetration of GDL into the channel affects the water discharge from the GDL as shown by Sasabe et al. [48] via X-ray radiography and by Turhan et al. [49] via neutron radiography. In addition, the GDL intrusion into the channel decreases the channel volume and consequently affects gas phase mass transport. A numerical investigation is needed to fully understand the effects of increased mass transport resistance under rib, under channel, and in channel due to a non-uniform compression pressure on a PEM fuel cell performance [50]. Incorporating the effects of non-uniform compression in numerical models will increase their accuracy for calculating a PEM fuel cell performance by the inclusion of: 1) porosity reduction

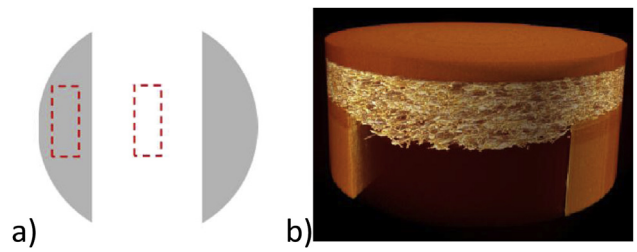


Fig. 11. a) Channel and rib representative areas configuration, and b) a TGP-H-120 Toray paper GDL visualization under channel/rib configuration.

under rib, 2) relative porosity increase under channel area, and 3) GDL intrusion into channel.

The third observation in Fig. 12 is that the GDL thickness under channel area slightly decreases at 2 MPa and then increases at 3 MPa in comparison with 1 MPa compression pressure case. As pressure applies to GDL, there are two competing factors influencing its thickness under channel. First, GDL thickness at under channel region far from channel (i.e., GDL bottom) decreases due to compressive pressure. Second, GDL thickness increases at regions near channel edge, as a result of non-uniform compression pressure and highly localized compression near the rib edge, which cause GDL material to bow and stretch into the channel area. The second factor is more prominent at 3 MPa compression pressure, leading to a thicker GDL under channel even at a higher compression. Strong deformation of GDL in a channel-rib configuration was also previously shown by the numerical stress analysis work of Serincan and Pasaogullari [51]. They showed that the deformation is toward the channel area and as a result of restricted motion at under rib area and significantly low Young modulus of GDLs in through thickness direction (0.5 MPa) compared to in-plane direction (9 GPa).

It is noted that Fig. 11 investigates the effect of the non-uniform compression pressures on an untreated TGP-H-120 Toray paper GDL. For treated GDLs, due to added PTFE, the stiffness of GDL increases i.e., there will be less resistance to compressive stresses [52]. Therefore, under a non-uniform compression pressure, GDL under rib regions experience less over-compression and GDL under channel experiences less intrusion into the channel. In other words, at a same compression pressure, a treated GDL's thickness and porosity change at channel and rib regions is expected to be less than the untreated one shown in Table 2. This means the effect of non-uniform compression pressure on an untreated GDL is more significant than treated GDLs. This needs future experiments to quantify the significances of non-uniform compression pressures for treated GDLs.

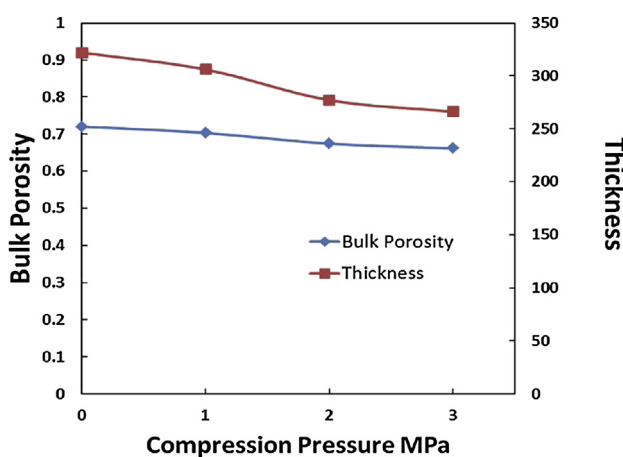


Fig. 10. Untreated TGP-H-120 bulk porosity and thickness variation with compression pressure.

## 5. Conclusions

We investigated the microstructure of a carbon paper GDL (Toray TGP-H-120) using the X-ray micro CT technique. The images obtained during the  $\mu$ XCT scans were further processed and the effects of binarization based on two different methods i.e. matching bulk porosity obtained via MIP, and Otsu's method were presented. It was found that the Otsu's method overestimate the GDL bulk porosity by 3.2%. The bulk porosity and porosity distributions were investigated for the GDL at different PTFE treatments and under uniform/non-uniform compression pressure. The results revealed the heterogeneous porosity distribution and anisotropy of the GDL microstructure. Heterogeneity is higher in through thickness direction compared to in-plane direction due to fiber orientation and increases with PTFE treatment. Bulk porosities and porosity distributions under rib area compared to under channel area were

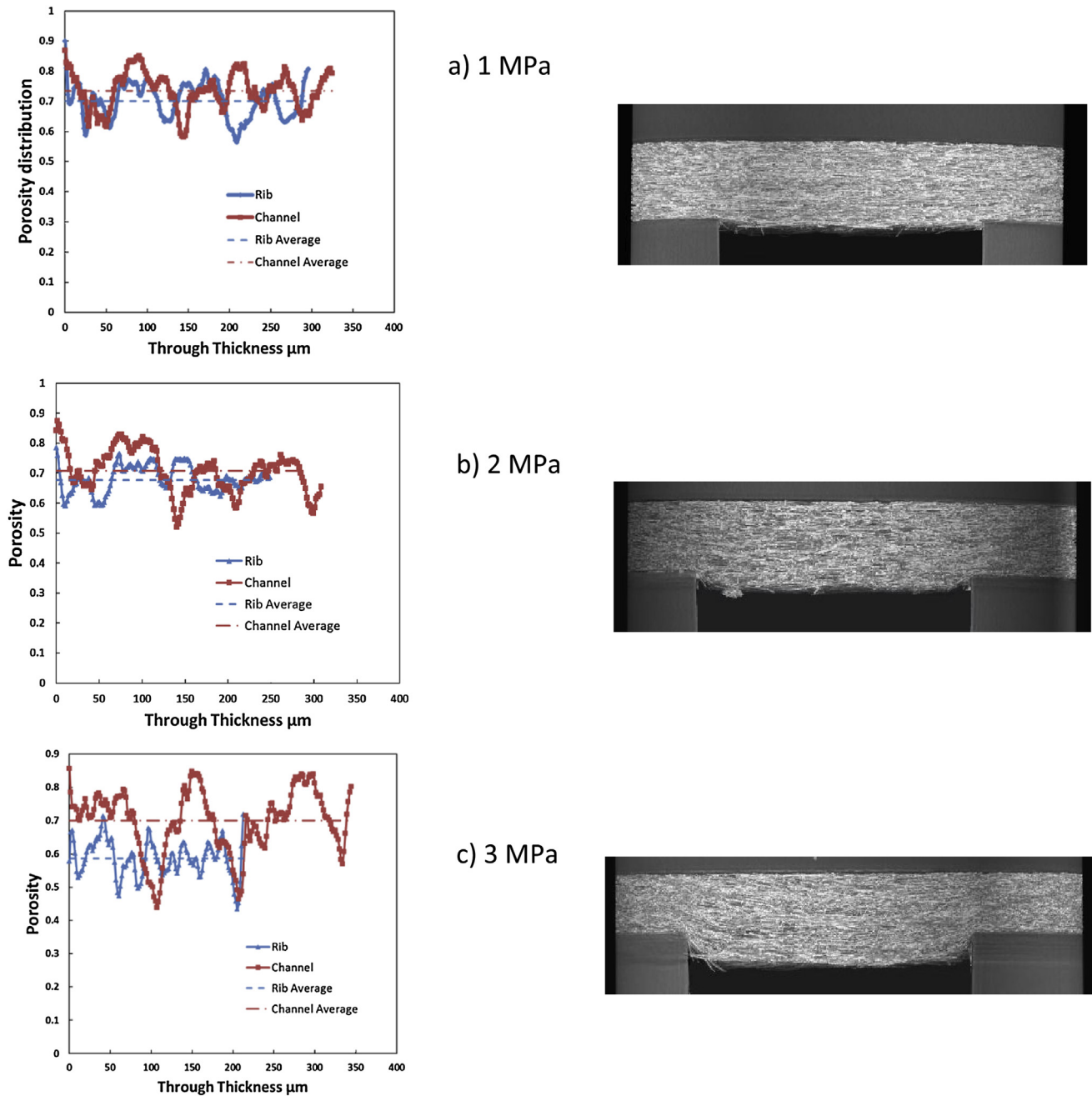


Fig. 12. Through thickness porosity distribution under rib and channel areas at different compression pressures, a) 1 MPa, b) 2 MPa, and c) 3 MPa.

**Table 2**  
Average porosity values under rib and channel at 0, 1, 2, and 3 MPa non-uniform compression pressure.

Compression pressure	0 MPa	1 MPa	2 MPa	3 MPa
Porosity (%)	Rib: 72.20 Channel: 72.20	Rib: 71.54 Channel: 73.40	Rib: 67.68 Channel: 71.00	Rib: 60.30 Channel: 70.00
Penetration length into the channel area (μm)	0	28	61	132

shown at various compression pressures. At 3 MPa, 16% reduction in average porosity from under channel to rib regions, significant change in porosity distribution, and a large penetration of GDL into the channel (132  $\mu\text{m}$ ) were observed. This present data is useful for PEFC numerical models to include the effects of PTFE treatment and non-uniform compression pressure in the study of transport phenomena in GDLs.

## References

- [1] J. Benziger, J. Nehls, D. Blackwell, T. Brennan, J. Itescu, *J. Membr. Sci.* 261 (2005) 98–106.
- [2] J. Ge, A. Higier, H. Liu, *J. Power Sources* 159 (2006) 922–927.
- [3] B. Thoben, A. Siebke, *J. New Mater. Electrochem. Syst.* 7 (2004) 13–20.

[4] N. Khajeh-Hosseini-Dalasm, K. Fushinobu, K. Okazaki, *Int. J. Hydrogen Energy* 35 (9) (2010) 4234–4246.

[5] H. Iwai, N. Shikazono, T. Matsui, H. Teshima, M. Kishimoto, R. Kishida, D. Hayashi, K. Matsuzaki, D. Kanno, M. Saito, H. Muroyama, K. Eguchi, N. Kasagi, H. Yoshida, *J. Power Sources* 195 (2010) 955–961.

[6] A. Sheidaei, M. Baniassadi, M. Banu, P. Askeland, M. Pahlavanpour, N. Kuuttila, F. Pourboghrat, L. Drzal, H. Garmestani, *Compos. Sci. Technol.* 80 (2013) 47–54.

[7] P. Shearing, J. Golbert, R.J. Chater, N.P. Brandon, *Chem. Eng. Sci.* 34 (2009) 3928.

[8] D. Gostovic, J.R. Smith, D.P. Kundinger, K.S. Jones, E.D. Wachsman, *Electrochem. Solid-State Lett.* 10 (12) (2007) B214–B217.

[9] C. Ziegler, S. Thiele, R. Zengerle, *J. Power Sources* 196 (2011) 2094–2097.

[10] H. Ostadi, P. Rama, Y. Liu, R. Chen, X. Zhang, K. Jiang, *J. Membr. Sci.* 351 (2010) 69–74.

[11] J.S. Cronin, Y.-C.K. Chen-Wiegert, J. Wang, S.A. Barnett, *J. Power Sources* 233 (2013) 174–179.

[12] A. Cecen, E.A. Wargo, A.C. Hanna, D.M. Turner, S.R. Kalidindi, E.C. Kumbur, *J. Electrochem. Soc.* 159 (3) (2012) B299–B307.

[13] S. Thiele, T. Fürstenhaupt, D. Banham, T. Hutzenlaub, V. Birss, C. Ziegler, R. Zengerle, *J. Power Sources* 228 (2013) 185–192.

[14] E. Wargo, V. Schulz, A. Cecen, S. Kalidindi, E. Kumbur, *Electrochim. Acta* 87 (2013) 201–212.

[15] A. Pfrang, D. Veyret, G.J. Janssen, G. Tsotridis, *J. Power Sources* 196 (2011) 5272–5276.

[16] F.N. Büchi, R. Flückiger, D. Tehlar, F. Marone, M. Stampanoni, *ECS Trans.* 16 (2) (2008) 587–592.

[17] Z. Fishman, J. Hinebaugh, A. Bazylak, *J. Electrochem. Soc.* 157 (11) (2010) B1643–B1650.

[18] Z. Fishman, A. Bazylak, *J. Electrochem. Soc.* 158 (8) (2011) B841–B845.

[19] J. Becker, R. Flückiger, M. Reum, F.N. Büchi, F. Marone, M. Stampanoni, *J. Electrochem. Soc.* 156 (10) (2009) B1175–B1181.

[20] J. James, H.-W. Choi, J. Pharoah, *Int. J. Hydrogen Energy* 37 (2012) I8216–I8230.

[21] W. Rasband, National Institutes of Health, Bethesda, Maryland, USA, 1997–2012 (online). Available: <http://imagej.nih.gov/ij/>.

[22] C. Schneider, W. Rasband, K. Eliceiri, *Nat. Meth.* 9 (2012) 671–675.

[23] M. Abramoff, P. Magalhaes, S.J. Ram, *Biophot. Int.* 11 (7) (2004) 36–42.

[24] T. Sasabe, G. Inoue, S. Tsushima, S. Hirai, T. Tokumasu, U. Pasaogullari, *ECS Trans.* 50 (2) (2012) 735–744.

[25] S. Zhang, R.E. Klimentidis, P. Barthelemy, *SCA Symp.* (2011). Paper #A080.

[26] T. Hara, E. Tanck, J. Homminga, R. Huiskes, *Bone* 31 (1) (2002) 107–109.

[27] R. Thiedemann, F. Fleischer, C. Hartnig, W. Lehnert, V. Schmid, *J. Electrochem. Soc.* 155 (4) (2008) B391–B399.

[28] N. Otsu, *IEEE Trans. Syst. Man. Cybern.* 9 (1) (1979) 62–66.

[29] M. Sezgin, B. Sankur, *J. Electron. Imaging* 13 (1) (2004) 146–165.

[30] *J. Power Sources* 108 (2002) 185–191.

[31] Y. Wang, C.-Y. Wang, *Electrochim. Acta* 50 (2005) 1307–1315.

[32] T.V. Nguyen, R.E. White, *J. Electrochem. Soc.* 140 (8) (1993) 2078–2186.

[33] N. Khajeh-Hosseini-Dalasm, K. Fushinobu, K. Okazaki, *J. Electrochem. Soc.* 157 (10) (2010) B1358–B1369.

[34] N. Akhtar, P. Kerkhof, *Int. J. Hydrogen Energy* 36 (2011) 5536–5549.

[35] B. Gao, T.S. Steenhuis, Y. Zevi, J.-Y. Parlane, R.N. Carter, T.A. Trabold, *J. Power Sources* 190 (2009) 493–498.

[36] U. Pasaogullari, P.P. Mukherjee, C.-Y. Wang, K.S. Chen, *J. Electrochem. Soc.* 154 (8) (2007) B823–B834.

[37] J. Pharoah, K. Karan, W. Sun, *J. Power Sources* 161 (2006) 214–224.

[38] H. Ju, *J. Power Sources* 191 (2009) 259–268.

[39] J. Feser, A. Prasad, S. Advani, *J. Power Sources* 162 (2006) 1226–1231.

[40] O. Burheim, P.J.S. Vie, J.G. Pharoah, S. Kjelstrup, *J. Power Sources* 195 (2010) 249–256.

[41] C. Lim, C. Wang, *Electrochim. Acta* 49 (2004) 4149–4156.

[42] V. Paganin, E. Ticianelli, E. Gonzalez, *J. Appl. Electrochem.* 26 (1996) 297–304.

[43] G.-H. Yoon, Y.-i. Park, *Int. J. Precis. Eng. Manuf.* 13 (7) (2012) 1153–1159.

[44] S. Litster, G. McLean, *J. Power Sources* 130 (2004) 61–76.

[45] L. Cindrella, A. Kannan, J. Lin, K. Saminathan, Y. Ho, C. Lin, J. Wertz, *J. Power Sources* 194 (2009) 146–160.

[46] G. Inoue, N. Ishibe, Y. Matsukuma, M. Minemoto, *ECS Trans.* 50 (2) (2012) 461–468.

[47] M.M. Tomadakis, S.V. Sotirchos, *AIChE J.* 37 (1) (1991) 74–86.

[48] T. Sasabe, S. Tsushima, S. Hirai, *Int. J. Hydrogen Energy* 35 (2010) 11119–11128.

[49] A. Turhan, S. Kim, M. Hatzell, M.M. Mench, *Electrochim. Acta* 55 (2010) 2734–2745.

[50] Y. Zhou, G. Lin, A.J. Shih, S.J. Hu, *J. Fuel Cell. Sci. Technol.* 6 (041005) (2009) 1–7.

[51] M.F. Serincan, U. Pasaogullari, *J. Power Sources* 196 (2009) 1314–1320.

[52] M.S. Ismail, A. Hassanpour, D.B. Ingham, L. Ma, M. Pourkashanian, *Fuel Cells* 12 (3) (2012) 391–397.